

Uncovering the presence or absence of photoluminescence from iron ions in crystals

Qiaoling Chen^{1,2,3,*}, Qianshan Quan,^{1,2,3} and Chang-Kui Duan^{1,2,3,4,†}

¹CAS Key Laboratory of Microscale Magnetic Resonance, and School of Physical Sciences, University of Science and Technology of China, Hefei 230026, China

²Anhui Province Key Laboratory of Scientific Instrument Development and Application, University of Science and Technology of China, Hefei 230026, China

³CAS Center for Excellence in Quantum Information and Quantum Physics, University of Science and Technology of China, Hefei 230026, China

⁴Hefei National Laboratory, University of Science and Technology of China, Hefei 230088, China



(Received 3 June 2024; accepted 28 August 2024; published 6 September 2024)

The poor understanding of the optical transitions and luminescent mechanisms critically hindered the development of near-infrared (NIR) Fe³⁺-activated phosphors, and efficient luminescence from Fe(Oh) has rarely been reported. In our study, we delve into these challenges and realize their correlation with the quenching mechanism of Fe³⁺ luminescence. First-principles calculations are utilized to analyze energy levels and electron-phonon coupling parameters, further elucidating potential deactivation pathways and factors influencing the occurrence of photoluminescence. A heuristic rule based on ligand-field strength, determined by the absorption wavelength of Cr³⁺ occupying the same octahedral site in oxides, is proposed to facilitate the prediction of both the potential and wavelength of Fe³⁺ emission. Our study offers consistent and reliable interpretations for the difficulties and challenges of iron-doped crystals, and provides valuable insights on the design and optimization of Fe³⁺-based phosphors.

DOI: [10.1103/PhysRevMaterials.8.095201](https://doi.org/10.1103/PhysRevMaterials.8.095201)

I. INTRODUCTION

The exploration of transition metal ions, specifically Fe³⁺, activated near-infrared (NIR) phosphors offers a compelling avenue in the development of environmentally friendly, chemically stable, and biocompatible optical materials [1–4] with applications ranging from plant growth and food analysis to biomedicine and night vision technologies [5–7]. However, achieving efficient Fe³⁺-based NIR phosphors remains challenging. Only a limited number of high-efficiency systems have been reported, such as the well-known LiGaO₂:Fe³⁺ [8,9] and LiGa₅O₈:Fe³⁺ [10–12], along with a few recently reported systems like the Sr_{2-y}Ca_y(InSb)_{1-z}Sn_{2z}O₆:Fe³⁺ [4] series, Sr₉Ga(PO₄)₇:Fe³⁺ [3], Li₂ZnSiO₄:Fe³⁺ [2], and KAl₁₁O₁₇:Fe³⁺ [1].

A significant barrier to the advancement of iron-containing phosphors is the poor understanding of the luminescence mechanisms, which involves site occupancy, valence states, and optical transition processes. EPR studies have revealed that Fe³⁺ ions occupy both tetrahedral and octahedral sites in various crystals [13–15], which will be referred to as Fe(Td) and Fe(Oh), respectively. However, for a significant period, only emissions peaking between 670–830 nm were observed, primarily attributed to Fe(Td) [16], albeit some emissions at similar ranges were tentatively associated with Fe(Oh). Considerable efforts have been dedicated to exploring the

luminescence of Fe³⁺ in octahedral sites, such as in α -Al₂O₃ [17], Ga₂O₃ [18], MgO [19], and LiGa₅O₈ [10,11,20]. Challenge increases with the interference of inevitable native defects and trace impurities.

In our recent work [16], we investigated the site occupancy and valence states of Fe³⁺ in solids, and further predicted their optical transition energies. In iron-doped normal spinel ZnAl₂O₄ crystal, EPR results indicate the presence of Fe³⁺ in octahedral and tetrahedral sites [15], which has also been supported by first-principles calculations [16]. Two emissions centered at around 445 nm and 745 nm were previously identified as originating from Fe(Td) and Fe(Oh) due to their high defect concentrations [15], but were reassigned to intrinsic defect and Fe(Td), respectively [16]. In the iron-doped yttrium gallium garnet, the zero-field splittings of the high-spin state of Fe(Oh) and Fe(Td) were interpreted [21], and the absorption spectra of both Fe(Td) and Fe(Oh) were confirmed [22]. However, only one emission peaked at ~805 nm was observed, which was attributed to the Fe(Td) [16], and the emission from Fe(Oh) was absent. Similar phenomena have been widely reported in other iron-doped crystals, such as LiAl₅O₈ and MAl₁₂O₁₉ ($M = \text{Ba, Sr, Ca}$) [20,23,24]. In the inverse spinel LiGa₅O₈, a weak luminescence with a sharp zero-phonon line at 1115 nm was observed. This was originally identified as Fe(Oh), but was later found to be associated with Ni²⁺ trace impurity based on the spectral features [16]. Therefore, the puzzling scarcity of efficient luminescence of systems activated by Fe(Oh) persists, especially given the EPR evidence confirming the site occupancy. More recently, luminescence around 1000 nm from Fe(Oh) has

*Contact author: cql@ustc.edu.cn

†Contact author: ckduan@ustc.edu.cn

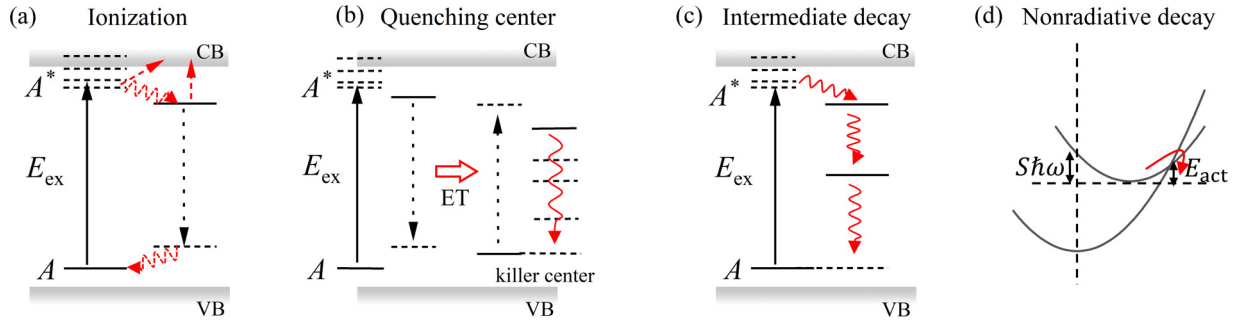


FIG. 1. Schematic illustrating luminescent quenching. (a) Electron thermal ionization to the conduction band, or hole to the valence band (not shown). (b) Energy transfer (ET) to a quenching center. (c) Sequential nonradiative decay via intermediate energy levels. (d) Multiphonon nonradiative relaxation.

been reported in hosts with weak ligand field, such as In^{3+} -, Sn^{4+} -, Lu^{3+} - and Mg^{2+} -based double-perovskite [4,25,26], Sc^{3+} -based $\text{NaScSi}_2\text{O}_6$ host [27], and Ga^{3+} -based structure confinement $\text{Sr}_9\text{Ga}(\text{PO}_4)_7$ hosts [3].

In this study, the energy level structures and electron-phonon coupling of iron in solids were detailed and discussed by combining first-principles calculations and the Tanabe-Sugano diagram analysis, and then the presence or absence nature of the photoluminescence from Fe^{3+} were uncovered. Ultimately, we have established a heuristic rule to aid in predicting the emission wavelength based on existing structural and luminescence data of other transition metal ions such as Cr^{3+} .

II. METHODS

First-principles calculations were performed based on the density functional theory (DFT) implemented in the Vienna *ab initio* simulation package code (VASP) [28,29]. The recommended projector augmented wave (PAW) method [30] was adopted to treat the interaction between ion core and electrons. The generalized gradient approximation of the Perdew-Burke-Ernzerhof (PBE) functional [31] was used for the exchange correlation functional. The conjugate gradient method was used to perform the geometric optimization until the Hellmann-Feynman forces on atoms less than $0.01 \text{ eV}/\text{\AA}$. The crystal hosts were optimized by an energy cutoff of 400 eV . The comparison of experimental and calculated lattice parameters were listed in Table S1 of the Supplemental Materials (SM) [32] (including Refs. [33–39]). The defect calculations were performed based on the supercell method.

In the DFT framework, some multiplet excited states are approximated by a combination of single determinants, which can be calculated by spin-multiplicity control or constrained occupancy methods. By calculations, the ${}^4\text{T}_1 \rightarrow {}^6\text{A}_1$ emissions of tetrahedral and octahedral Fe^{3+} in a series of hosts can well reproduce the experimental results, and the basic parameters Δ and B have been studied in comparison with experiments in our previous work [16]. Here we further consider ${}^2\text{T}_2$ excited states to discuss the presence or absence nature of photoluminescence of Fe^{3+} in solids. The main components, calculational details, and their Coulomb interactions of ${}^4\text{T}_1$ and ${}^2\text{T}_2$ excited states are elaborately discussed in Note S1 of the SM [32] for Fe^{3+} activators with $3d^5$ electronic configuration. The excited states and optical transition energies

were calculated by combing first-principles calculations based on hybrid HSE06 functionals and Tanabe-Sugano theory. As a compromise between accuracy and computational resources of hybrid functional calculations, only one Γ -centered point was used to sample the Brillouin zone for the defect calculations in supercells. The convergence test of our calculational method have been performed [16].

III. RESULTS AND DISCUSSIONS

A. First-principles calculations on excited states

Figure 1 outlines the mechanisms of luminescent quenching in solids. The mechanism in Fig. 1(a) is generally ruled out due to the much higher energy of the charge transfer excited state ($\text{Fe}^{2+} + h_{\text{VBM}}$ or $\text{Fe}^{4+} + e_{\text{CBM}}$, by over 2 eV) compared to the ${}^4\text{T}_1$ states in many systems with luminescence being absent [16]. De-excitation via energy transfer to quenching centers, as shown in Fig. 1(b), can be controlled through experimental designing and is thus excluded from consideration, given the general nature of the quenching. Concerning the mechanism illustrated in Fig. 1(c), the competition of low-spin ($S = 1/2$) and high-spin ($S = 5/2$) states of iron compounds in earth's mantle under pressure has led us to consider the possible involvement of the intermediate low-spin states of Fe^{3+} dopants in relaxation processes [40]. These low-spin states of Fe^{3+} in solids are not observable in absorption spectra, as their forced electric-dipole transitions are more thoroughly spin-forbidden than $S = 3/2$ states. Therefore, first-principles calculations for the energy levels of Fe^{3+} in solids become necessary.

We choose MgAl_2O_4 as a prototype host. EPR and first-principles calculations show the presence of Fe^{3+} at both octahedral and tetrahedral sites in these spinels. However, there was only one emission peaked at $\sim 700 \text{ nm}$ from $\text{Fe}(\text{Td})$, and the emission from $\text{Fe}(\text{Oh})$ was absent in experiments [41]. Here, we focus on the energy levels, excited-state relaxations, and optical processes of octahedrally coordinated Fe^{3+} by first-principles calculations. The optical transitions of tetrahedrally coordinated Fe^{3+} have been discussed in our previous work [16]. ${}^6\text{A}_1$ ground state and ${}^4\text{T}_1$ excited state are separately calculated by spin multiplet setting with $|\xi\eta\zeta\theta\epsilon\rangle$ and $|\theta\xi\eta\zeta\bar{\zeta}\rangle$ electronic configurations, where ξ, η, ζ are the components of t_2 orbitals, and θ, ϵ are the components of e orbitals [42]. At the ground-state equilibrium structure, labeled as $Q({}^6\text{A}_1)$, the ${}^4\text{T}_1$ state is 0.86 eV higher than the ${}^6\text{A}_1$ state.

The emission energy ${}^4T_1 \rightarrow {}^6A_1$ is calculated as 0.65 eV, and the thermal activation energy to reach the ${}^4T_1 - {}^6A_1$ crossover point is 0.44 eV, too high to convincingly explain the lack of luminescence due to the nonradiative decay in Fig. 1(d). Then we consider the lowest spin doublet excited state 2T_2 by $|\xi\eta\zeta\bar{\xi}\bar{\eta}\rangle$ electronic configuration. 2T_2 and 4T_1 states are comparable in energy in our direct calculations. At the $Q({}^6A_1)$ geometric structure, the 2T_2 state is 0.95 eV above the 6A_1 ground state, and the activation energy of 2T_2 , as determined by the intersection of its potential curve with that of the 6A_1 , is only about 0.20 eV.

The energy of the ${}^4A_1/{}^4E$ state relative to the ground state 6A_1 is dominated by the Coulomb interaction and almost independent of the ligand-field splitting. The calculated energies of ${}^4A_1/{}^4E$ are usually underestimated by about 0.1 eV with respect to the experimental results [16], showing the underestimation of the Coulomb interaction in calculations. Regarding the energy of the Fe^{3+} 's 4T_1 state, both the underestimation of Coulomb interaction and the spin contamination [43] contribute to its energy being underestimated. Comparison to experimental results indicates that the energies of 4T_1 for $Fe(Oh)$ are underestimated by less than or about 0.1 eV [16].

It is necessary to consider the mixing of different Slater determinants due to the Coulomb interaction, i.e., configuration interaction. In principle, the electronic charge density rearrangements of the exact excited states induced by the configuration interaction are influenced by the wavefunction mixing of different Slater determinants with different electronic occupancy. Neglecting this interaction leads to a minor overestimation of the energy of 4T_1 , but significantly overestimates the energy of 2T_2 . In detail, the energies under single Slater determinant approximation are $E({}^4T_1[t_2^4({}^3T_1)e]) - E({}^6A_1) = 10B + 6C - \Delta$ and $E({}^2T_2[t_2^5]) - E({}^6A_1) = 15B + 10C - 2\Delta$ [44]. However, the mixing with $t_2^4({}^3T_1)e$ and $t_2^3({}^2T_2)e^2({}^1A_1)$ due to Coulomb interaction significantly downshifts the 2T_2 level by about $3.42B$ by using $\Delta \sim 27B$, $C/B \sim 5$ [44]. Meanwhile, the configuration interaction only leads to a downshift of ${}^4T_1[t_2^4({}^3T_1)e]$ by around $0.81B$ [44] (refer to Note S1 in the SM [32] for details). After these corrections, at the $Q({}^6A_1)$ geometric structure, 2T_2 is shifted to 0.64 eV above the 6A_1 ground level, which is 0.16 eV lower than the corrected 4T_1 .

Besides, the impact of electron-phonon coupling is discussed, as shown in Fig. 2. The total Huang-Rhys (HR) factors are respectively 1.93 and 3.54 for 4T_1 and 2T_2 states, with corresponding Stokes shifts of 0.21 eV and 0.41 eV, which are notably larger for 2T_2 . 2T_2 exhibits a more significant coupling with high-energy phonons compared to 4T_1 . Hence, 2T_2 provides the intermediate state to quench the excited $Fe(Oh)$.

Finally, the potential energy surfaces of Fe^{3+} are depicted in Fig. 3. An excited Fe^{3+} thermalizes quickly to the 4T_1 states at $Q({}^4T_1)$ geometry, and then nonradiatively relaxes to the 2T_2 state, which is lower in energy, has a higher electron-phonon coupling strength, and involves coupling with high-energy phonons more than 4T_1 . Subsequently, Fe^{3+} is nonradiatively relaxed from 2T_2 at $Q({}^2T_2)$ to the 6A_1 ground state. Hence, the favorable ${}^2T_2 \leftrightarrow {}^6A_1$ nonradiative relaxation makes 2T_2 an efficient intermediate state for the quenching mechanism as illustrated in Fig. 1(c).

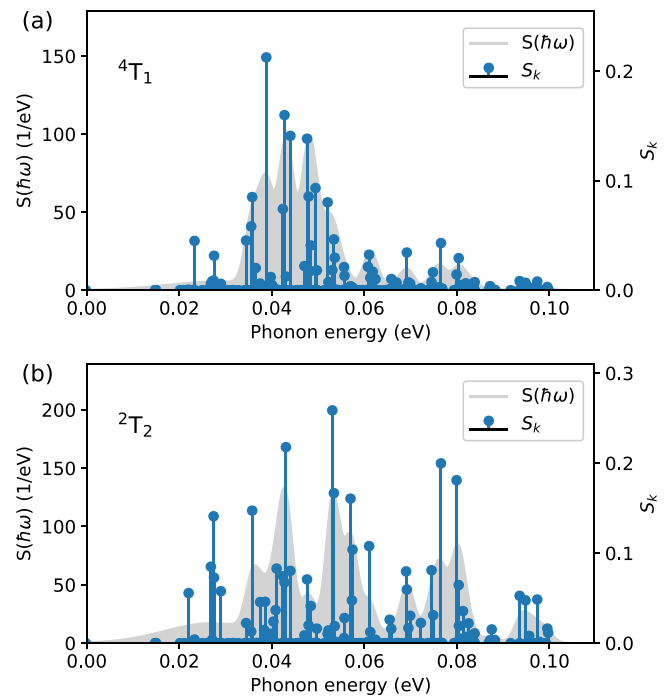


FIG. 2. Partial HR factors (S_k) of the 4T_1 (a) and 2T_2 (b) states of Fe^{3+} in $MgAl_2O_4$. The shaded regions [$S(\hbar\omega)$] represent the convolutions of the sticks with a full width at half maximum of 0.01 eV to guide eyes.

B. Energy levels based on the Tanabe-Sugano diagram

Here we discuss the excited energy levels of Fe^{3+} determined by the Tanabe-Sugano theory based on the ligand-field parameter Δ for $e-t_2$ splitting, alongside the Racah parameter, B and C . Utilizing the free-ion value for the ratio of the Racah parameter, i.e., $C/B = 4.73$, and using B as the energy unit, the Tanabe-Sugano diagram for the energy levels of Fe^{3+} is depicted in Fig. 4(a). It's worth noting that for the $Fe(Td)$, the electron-hole duality of d^5 is employed to make Δ positive. In Fig. 4(a), we observed that as the ligand-field strength increases, the energy of the 4T_1 state decreases almost linearly, while the 2T_2 energy experiences an even sharper decrease, approximately twice as much as the former. The luminescent quenching by 2T_2 intermediate energy level would be severe for Fe^{3+} in the lattice site with large ligand field strength. The critical ligand-field strength of comparable 4T_1 with 2T_2 state is predicted as $\Delta/B \approx 21$ in Fig. 4(a).

The Δ , B , and Δ/B values of tetrahedral and octahedral Fe^{3+} activator in the experimentally reported hosts have been detailed calculated and shown in Table I and Fig. 4(a). B is only weakly dependent on host in oxides, and the energy levels dominate by the ligand field strength Δ . The tetrahedral Fe^{3+} in oxides show a small Δ/B ranging from 11–13, while the Δ/B values of octahedral ones are much higher ranging from 16–27, depending on the crystal host structures and ionic radii. Thus, the luminescence of tetrahedral Fe^{3+} in oxides is potentially observable due to small Δ/B , unless suppressed by factors like structure relaxation in soft crystals, strong ionization, or unidentified quenching centers, while the occurrence of luminescence of octahedral Fe^{3+} is rigorous. For the

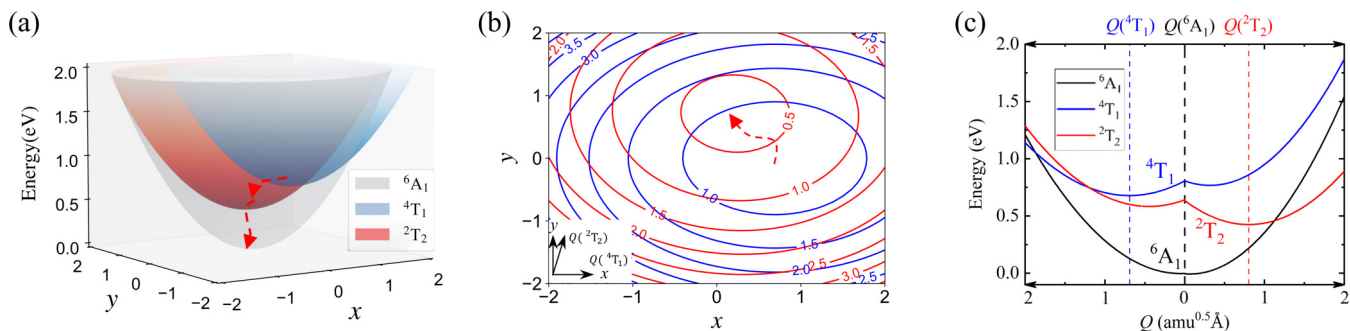


FIG. 3. (a) Configuration coordinate diagram surfaces of the Fe^{3+} 's ground state ${}^6\text{A}_1$, and excited states ${}^4\text{T}_1$ and ${}^2\text{T}_2$. (b) Contour lines of potential energies for the excited states ${}^4\text{T}_1$ (blue) and ${}^2\text{T}_2$ (red), delineated on the x - y plane encompassing their displacements. (c) One-dimensional configurational coordinate diagram along equilibrium configurations $Q({}^4\text{T}_1) \rightarrow Q({}^6\text{A}_1) \rightarrow Q({}^2\text{T}_2)$, where mass-weighted displacements x , y , and Q are given in units of $\sqrt{\text{amu}}\text{\AA}$, with “amu” the atomic mass unit.

large Δ/B case, generally at octahedral sites, the luminescence would possibly be quenched through intermediate ${}^2\text{T}_2$ excited states.

Among the lattice sites without reported luminescence from Fe^{3+} , the Δ/B value of $\text{Fe}(\text{Oh})$ in the MgAl_2O_4 host is the largest and that of $\text{Fe}(\text{Oh})$ in the $\text{Y}_3\text{Ga}_5\text{O}_{12}$ (YGG) host is the smallest; while among the hosts with observable Fe^{3+} luminescence, the Δ/B value of $\text{Fe}(\text{Oh})$ in the CaSnO_3 host is the largest. Generally, with small Δ/B value, the luminescence would potentially occur. We then discuss the above three typical cases based on Tanabe-Sugano theory.

For $\text{Fe}(\text{Oh})$ in MgAl_2O_4 , the parameters Δ , B , and their ratio are calculated as 2.05 eV, 0.076 eV, and 27.0, respectively. ${}^2\text{T}_2$ excited state is significantly lower than the ${}^4\text{T}_1$, leading to luminescent quenching. In contrast, the ${}^2\text{T}_2[t_2^5]$ and ${}^4\text{T}_1[t_2^4({}^3\text{T}_1)e]$ levels under single-Slater-determinant approximation, plotted as dotted lines, are closer to each other in energy, highlighting the importance of configuration interaction. It is noted that the parameter B can be estimated using the calculated energy of ${}^4\text{T}_1$ or ${}^4\text{A}_1$, with $E({}^4\text{T}_1 - {}^6\text{A}_1) = (10 + 6C/B)B - \Delta$ and $E({}^4\text{A}_1 - {}^6\text{A}_1) = (10 + 5C/B)B$, respectively. However, due to the strong ligand field, obtaining

the energy of the ${}^4\text{A}_1$ state via the occupation matrix control methodology with spin quartet setting has proven challenging, as it tends to relax to ${}^4\text{T}_1$ with much lower energy. Hence, we employ $B = [E({}^4\text{T}_1 - {}^6\text{A}_1) + \Delta]/(10 + 6C/B)$ with the ratio $C/B = 4.73$. The parameters Δ , B , and Δ/B can also be obtained from experimentally measured absorption or excitation spectra based on the correct energy level assignment. The $d \leftrightarrow d$ interconfigurational excitations of octahedral Fe^{3+} should be much weaker than that of tetrahedral Fe^{3+} due to the further forbidden by even parity, and the former was rarely reported, except the case in the YGG host in the following paragraph. For $\text{Fe}(\text{Td})$, the parameters were fitted by experimental absorption spectra at low temperature in the YGG host as $\Delta = 0.81$ eV, $B = 0.092$ eV, and $C = 0.317$ eV [22], comparable with our calculational results in Table I. In the $\text{Mg}_2\text{Al}_4\text{Si}_5\text{O}_{18}\text{-Al}_2\text{O}_3\text{-MgAl}_2\text{O}_4\text{-SiO}_2$ host, the parameters were fitted as $\Delta = 1.01$ eV, $B = 0.067$ eV, and $C = 0.365$ eV [48]. In the Zn_2SiO_4 host, the parameters of tetrahedral Fe^{3+} were $\Delta = 0.92$ eV, $B = 0.066$ eV, and $C = 0.391$ eV according to the low temperature excitation spectra [49]. The experimentally fitted ligand field strength and Racah parameter B of Fe^{3+} at tetrahedral Mg^{2+} or Zn^{2+} are

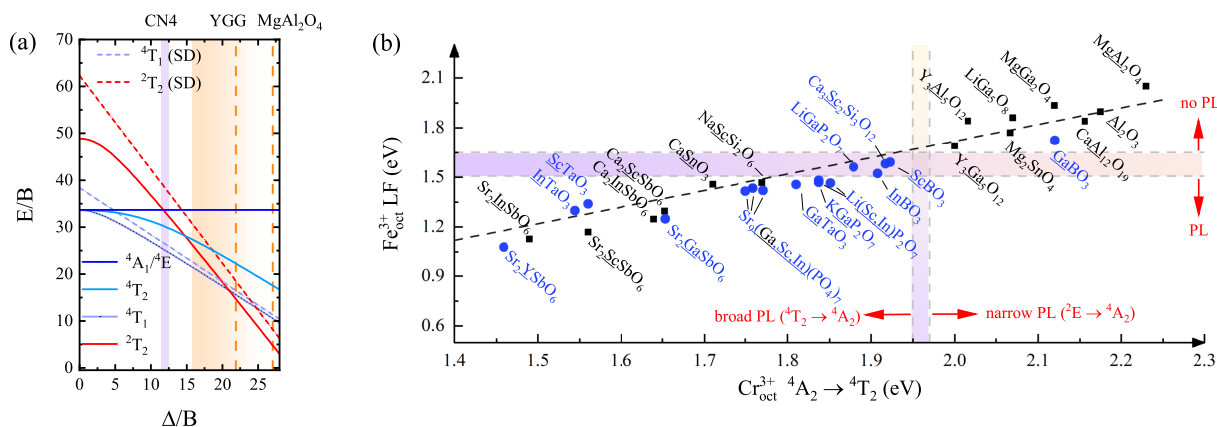


FIG. 4. (a) Tanabe-Sugano diagram of Fe^{3+} ($3d^5$), with Δ/B value ranges of tetrahedrally (light purple) and octahedrally (orange) coordinations marked. ${}^4\text{T}_1(\text{SD})$ and ${}^2\text{T}_2(\text{SD})$ curves present energies calculated with single Slater determinants. (b) Calculated ligand-field strength of $\text{Fe}^{3+}_{\text{oct}}$ versus measured excitation peak of $\text{Cr}^{3+}_{\text{oct}}$, with a dashed line $y = x - 0.28$ (eV) plotted to guide eyes. Filled squares denote experimentally studied systems.

TABLE I. Δ (eV), B (eV), Δ/B values, and emission energies (eV) of Fe^{3+} in various tetrahedral and octahedral lattice sites.

		Δ	B	Δ/B	Emission
LiGa_5O_8	Fe(Td)	0.79	0.069	11.6	1.84 [11,12]
LiAl_5O_8	Fe(Td)	0.89	0.072	12.4	1.70–1.80 [10,11]
$\text{Y}_3\text{Al}_5\text{O}_{12}$	Fe(Td)	0.85	0.069	12.3	1.58 [45,46]
$\text{Y}_3\text{Ga}_5\text{O}_{12}$	Fe(Td)	0.82	0.069	12.0	1.54 [21,46]
$\text{Lu}_3\text{Ga}_5\text{O}_{12}$	Fe(Td)	0.85	0.070	12.2	1.50 [46]
MgAl_2O_4	Fe(Td)	0.89	0.070	12.7	1.73 [41]
$\text{Sr}_2\text{InSbO}_6$	Fe(Oh)	1.13	0.068	16.6	1.40 [4]
$\text{Sr}_2\text{ScSbO}_6$	Fe(Oh)	1.17	0.069	17.0	1.37 [47]
$\text{Ca}_2\text{InSbO}_6$	Fe(Oh)	1.25	0.069	17.9	1.33 [4]
$\text{Ca}_2\text{ScSbO}_6$	Fe(Oh)	1.30	0.070	18.6	1.30 [47]
CaLaMgSbO_6	Fe(Oh)	1.44	0.077	18.7	1.25 [25]
$\text{Sr}_9\text{Ga}(\text{PO}_4)_7$	Fe(Oh)	1.44	0.074	19.4	1.36 [3]
CaSnO_3	Fe(Oh)	1.46	0.072	20.1	1.23 [4]
$\text{Y}_3\text{Ga}_5\text{O}_{12}$	Fe(Oh)	1.69	0.077	21.9	
$\text{Y}_3\text{Al}_5\text{O}_{12}$	Fe(Oh)	1.77	0.076	23.3	
LiGa_5O_8	Fe(Oh)	1.86	0.075	24.7	
LiAl_5O_8	Fe(Oh)	1.95	0.074	26.4	
MgAl_2O_4	Fe(Oh)	2.05	0.076	27.0	

consistent with our calculations presented in Table I. For Fe^{3+} at the octahedral site in the $\text{Sr}_9\text{Ga}(\text{PO}_4)_7$ host, $\Delta = 1.38$ eV, $B = 0.080$ eV, and $C = 0.376$ eV have been obtained by fitting experimental excitation spectra, and are comparable with our calculations [3].

For the case of $\text{Fe}(\text{Oh})$ in YGG, the ligand-field strength Δ is calculated as 1.69 eV, and the estimated value of B is 0.077 eV. Consequently, the ratio of Δ/B is determined to be 21.9. In comparison, fitting the experimental absorption spectrum from $S = 5/2$ to $S = 3/2$ states leading to $\Delta = 1.62$ eV, $B = 0.066$ eV, and $C = 0.384$ eV [22]. Therefore, $\text{Fe}(\text{Oh})$ exists in MgAl_2O_4 and YGG without producing NIR emission with a large Δ/B , consistent with the first-principles calculations complemented by configuration interaction correction with lower level energy and larger electron-phonon coupling of 2T_2 than 4T_1 states, as discussed in the following section.

Conversely, for the case of $\text{Fe}(\text{Oh})$ in CaSnO_3 , the parameters Δ , B , and their ratio are calculated as 1.46 eV, 0.072 eV, and 20.1, respectively. $\text{Fe}(\text{Oh})$ in CaSnO_3 was reported to emit NIR light with a relatively small Δ/B , also consistent with our calculations of higher 2T_2 than 4T_1 by 0.19 eV. If the Δ/B value is lower than that in CaSnO_3 , the luminescence from Fe^{3+} would be potentially observable, unless suppressed by other factors such as large structure relaxation in soft crystals, strong ionization, or unexpected quenching centers.

As B is only weakly dependent on host in oxides (data in Table S3 in SM [32]), a critical (upper) ligand-field strength of 1.60 eV is estimated for the presence of photoluminescence using the typical value $B \approx 0.076$ eV. This critical value varies within the range of 1.50–1.70 eV for $C/B \sim 4$ –5 and $E({}^4A_1 - {}^6A_1) = (10 + 5C/B)B \sim 2.5$ –2.7 eV. Furthermore, the larger relaxation energy of 2T_2 compared to 4T_1 results in a decrease in the critical value. Using MgAl_2O_4 as a reference, this decrease is estimated to be about 0.1 eV.

C. Connection between Fe^{3+} and Cr^{3+} optical transitions

Finally, we explore a series of crystal hosts for the potential luminescence of octahedrally coordinated Fe^{3+} by connecting it with Cr^{3+} activators. These hosts include spinels, garnets, tantalates, double-perovskites, stannates, borates, and phosphates. Figure 4(b) illustrates a linear relationship between the ligand-field strength Δ of Fe^{3+} and the experimentally observed excitation of Cr^{3+} . Notably, the latter is primarily determined by the Δ associated with $\text{Cr}_{\text{oct}}^{3+}$. The smaller Δ value for $\text{Fe}_{\text{oct}}^{3+}$ compared to that of $\text{Cr}_{\text{oct}}^{3+}$ can be attributed to the reduced effective radius of the d orbital in the former.

In spinels AB_2O_4 and inverse spinels $\text{Li}B_5O_8$ ($A = \text{Zn}$, Mg ; $B = \text{Ga}$, Al), octahedrally coordinated Cr^{3+} ions exhibit sharp ${}^2E \rightarrow {}^4A_2$ emissions at wavelengths around 700 nm and the first excitation peak is in the range of 2.05 to 2.35 eV [50–53]. The energy of 4T_2 is higher than 2E as a result of the large ligand-field strength of Cr^{3+} , resulting in the observed sharp emission from 2E . For Fe^{3+} ions, the large ligand-field strength leads to lowering of 2T_2 to underneath 4T_1 , providing the pathway for the nonradiatively relaxation and quenching the 4T_1 emission. Therefore, in these hosts, only emission of $\text{Fe}(\text{Td})$ (where $\Delta_{\text{Fe}^{3+}} < 1$ eV) has been reported, while that of Fe^{3+} from the octahedral site (where $\Delta_{\text{Fe}^{3+}} > 1.7$ eV) is absent. It's worth noting that previously reported near-infrared emission beyond $1 \mu\text{m}$ from $\text{Fe}(\text{Oh})$ in the LiGa_5O_8 host has been clarified as Ni^{2+} impurities [16]. The poorly understanding of luminescent and quenching process of Fe^{3+} ions leads to massive efforts for luminescence from $\text{Fe}(\text{Oh})$ [54,55].

Recently, researchers have been searching near-infrared emission about $1 \mu\text{m}$ in perovskites. In perovskites such as CaSnO_3 , $(\text{Ca}/\text{Sr})_2\text{InSbO}_6$, $(\text{Ca}/\text{Sr})_2\text{LaLiTeO}_6$, and CaLaMgSbO_6 , the calculated $\Delta_{\text{Fe}^{3+}}$ at the octahedral site falls in the range of 1.13–1.46 eV. This results in a higher 2T_2 and shorter ${}^4T_1 \rightarrow {}^6A_1$ emission wavelength compared to that of the octahedral sites in spinels and garnets. The luminescence of $\text{Fe}(\text{Oh})$ falls within 1.23–1.40 eV [4,25]. Meanwhile, Cr^{3+} in $\text{Sr}_2\text{InSbO}_6$, which has a relatively small ligand-field strength, was reported to emit broad NIR light of ${}^4T_2 \rightarrow {}^4A_2$ transition [56]. Furthermore, in $\text{NaScSi}_2\text{O}_6$, the value of $\Delta_{\text{Fe}^{3+}}$ is 1.47 eV, comparable to that in perovskites. However, due to weak covalent bonding, the Racah parameter is larger, resulting in an emission energy that is higher by about 0.14 eV.

In the $A_3B_2C_3O_{12}$ garnet series ($B = \text{Al}$, Ga , Sc , In), the emission of Cr^{3+} evolves from the sharp R -line emission of ${}^2E \rightarrow {}^4A_2$ transition in a strong ligand field to the broad band emission of the ${}^4T_2 \rightarrow {}^4A_2$ transition in a weak field. This evolution occurs when Al^{3+} or Ga^{3+} at the B site, where Cr^{3+} resides, is replaced by Sc^{3+} or In^{3+} ions [57–62]. For iron doping, the $\Delta_{\text{Fe}^{3+}}$ values at octahedral B sites are around the critical ligand-field strength, 1.77 eV in $\text{Y}_3\text{Al}_5\text{O}_{12}$ and 1.69 eV in $\text{Y}_3\text{Ga}_5\text{O}_{12}$ hosts. Experimentally, no luminescence from $\text{Fe}(\text{Oh})$ has been observed. The ligand-field strength can be modified by ion regulation, where the $\Delta_{\text{Fe}^{3+}}$ value changes from 1.64 to 1.58, 1.55, 1.46, and then 1.40 eV in $\text{Ca}_3\text{Ga}_2\text{Si}_3\text{O}_{12}$, $\text{Ca}_3\text{Sc}_2\text{Si}_3\text{O}_{12}$, $\text{Ca}_3\text{In}_2\text{Si}_3\text{O}_{12}$, $\text{Sr}_3\text{In}_2\text{Si}_3\text{O}_{12}$, and $\text{Sr}_3\text{In}_2\text{Ge}_3\text{O}_{12}$ hosts, respectively. The luminescence from tetrahedral and octahedral Fe^{3+} in large A , B , and C

ion systems can be further studied for dual-mode optical devices.

Finally, we discuss the phosphates $\text{Sr}_9M(\text{PO}_4)_7$ [63] and LiMP_2O_7 [64], as well as the tantalates $M\text{Ta}_2\text{O}_6$ and borates $M\text{BO}_3$ ($M = \text{Ga}, \text{Sc}, \text{In}$). It has been reported that Cr^{3+} in $\text{Sr}_9M(\text{PO}_4)_7$ crystals exhibit ${}^4\text{T}_2 \rightarrow {}^4\text{A}_2$ broad emissions due to structure confinement [63]. Calculations obtain $\Delta_{\text{Fe}^{3+}} = 1.42\text{--}1.44$ eV and predict the possible luminescence of Fe^{3+} at site M , which has been confirmed experimentally for $M = \text{Ga}$ [3]. Similar structure confinement has been noted in LiMP_2O_7 crystals, where Fe^{3+} is predicted to emit NIR light with $\Delta_{\text{Fe}^{3+}} = 1.46\text{--}1.56$ eV in LiMP_2O_7 ($M = \text{Ga}, \text{Sc}, \text{In}$). Furthermore, the change in emission energies of Cr^{3+} along $M = \text{Ga}, \text{Sc}, \text{In}$ in tantalates and borates is more pronounced compared to that in LiMP_2O_7 and $\text{Sr}_9M(\text{PO}_4)_7$. In borates, the primary Cr^{3+} emission changes from a sharp ${}^2\text{E} \rightarrow {}^4\text{A}_2$ emission in GaBO_3 to broad ${}^4\text{T}_2 \rightarrow {}^4\text{A}_2$ transitions in ScBO_3 and InBO_3 [65,66]. Meanwhile, the primary emission remains ${}^4\text{T}_2 \rightarrow {}^4\text{A}_2$ in $M\text{TaO}_3$ ($M = \text{Ga}, \text{Sc}, \text{In}, \text{Lu}$) [67,68]. Our calculations yield the ligand-field strengths of $\Delta_{\text{Fe}^{3+}}$ as 1.73, 1.59, 1.53 eV in $M\text{BO}_3$ and 1.45, 1.34, 1.30 eV in $M\text{TaO}_3$ for $M = \text{Ga}, \text{Sc}, \text{In}$, respectively. Consequently, while the luminescence of Fe^{3+} is potentially observable in $M\text{TaO}_3$, it should be absent in GaBO_3 . Furthermore, since the predicted ligand field strengths are near the threshold, experimental exploration is necessary to determine if Fe^{3+} in octahedral site emits in LiMP_2O_7 , ScBO_3 , and InBO_3 .

The comparative discussion on Cr^{3+} and Fe^{3+} shows that in hosts where octahedral Cr^{3+} sites exhibit high-efficiency broadband NIR emission, attributed to ${}^4\text{T}_2 \rightarrow {}^2\text{A}_2$ transition as a result of weak ligand field, there is a tendency for NIR emission from the $\text{Fe}(\text{Oh})$ at around 900 nm or longer wavelengths.

IV. CONCLUSIONS

Our comprehensive theoretical analysis, based on first-principles calculations on Fe^{3+} ions in solids, has elucidated that the primary factor determining the presence or absence of luminescence for $\text{Fe}(\text{Oh})$ is the host-dependent ligand-field strength. Additional contributions come from the nephelauxetic effect on the Coulomb interaction and the electron-phonon coupling. Specifically, the ${}^2\text{T}_2$ level descends below the ${}^4\text{T}_1$ level when the ligand field surpasses a critical value (approximately 1.5 to 1.7 eV), enabling a nonradiative relaxation pathway that suppresses the luminescence. Conversely, in cases of weak ligand field, particularly for $\text{Fe}(\text{Oh})$ replacing ions with large ion radii (e.g., $\text{Sc}, \text{In}, \text{Lu}, \text{Y}$), NIR luminescence is anticipated. Additionally, we have established a heuristic rule, depicted in Fig. 4(b), for predicting the emission potential of $\text{Fe}(\text{Oh})$ and estimating its emission wavelength based on the absorption wavelength of Cr^{3+} occupying the same octahedral site, for which extensive data are available across various hosts.

ACKNOWLEDGMENTS

This work was supported by the Innovation Program for Quantum Science and Technology (Grant No. 2021ZD0302200), the National Natural Science Foundation of China (Grants No. 12474242 and No. 62375255), and University Science Research Project of Anhui Province (Grant No. KJ2020A0820). The numerical calculations were performed on the supercomputing system at the Supercomputing Center of the University of Science and Technology of China.

- [1] G. Liu, S. Zhang, and Z. Xia, Multi-sites energy transfer in Fe^{3+} -doped $\text{KAl}_{11}\text{O}_{17}$ phosphor toward zero thermal quenching near-infrared luminescence, *Opt. Lett.* **48**, 1296 (2023).
- [2] Y. Yang, L. Shen, J. Zhang, S. Zhao, Q. Pang, X. Zhang, P. Chen, and L. Zhou, Tetracoordinate Fe^{3+} activated Li_2ZnAO_4 ($A = \text{Si}, \text{Ge}$) near-infrared luminescent phosphors, *Inorg. Chem.* **62**, 12862 (2023).
- [3] F. Zhao, Y. Shao, Z. Song, and Q. Liu, Structural confinement toward suppressing concentration and thermal quenching for improving near-infrared luminescence of Fe^{3+} , *Inorg. Chem. Front.* **10**, 6701 (2023).
- [4] D. Liu, G. Li, P. Dang, Q. Zhang, Y. Wei, L. Qiu, M. S. Molokeev, H. Lian, M. Shang, and J. Lin, Highly efficient Fe^{3+} -doped $\text{A}_2\text{BB}'\text{O}_6$ ($A = \text{Sr}^{2+}, \text{Ca}^{2+}$; $B, B' = \text{In}^{3+}, \text{Sb}^{5+}, \text{Sn}^{4+}$) broadband near-infrared-emitting phosphors for spectroscopic analysis, *Light Sci. Appl.* **11**, 112 (2022).
- [5] Y. Wei, P. Dang, Z. Dai, G. Li, and J. Lin, Advances in near-infrared luminescent materials without Cr^{3+} : Crystal structure design, luminescence properties, and applications, *Chem. Mater.* **33**, 5496 (2021).
- [6] M.-H. Fang, T.-Y. Li, W.-T. Huang, C.-L. Cheng, Z. Bao, N. Majewska, S. Mahlik, C.-W. Yang, K.-M. Lu, G. Leniec, S. M. Kaczmarek, H.-S. Sheu, and R.-S. Liu, Surface-protected high-efficiency nanophosphors via space-limited ship-in-a-bottle synthesis for broadband near-infrared mini-light-emitting diodes, *ACS Energy Lett.* **6**, 659 (2021).
- [7] A. Guelpa, F. Marini, A. du Plessis, R. Slabbert, and M. Manley, Verification of authenticity and fraud detection in South African honey using NIR spectroscopy, *Food Control* **73**, 1388 (2017).
- [8] Z. Zhou, X. Yi, P. Xiong, X. Xu, Z. Ma, and M. Peng, Cr^{3+} -free near-infrared persistent luminescence material $\text{LiGaO}_2:\text{Fe}^{3+}$: optical properties, afterglow mechanism and potential bioimaging, *J. Mater. Chem. C* **8**, 14100 (2020).
- [9] A. K. Somakumar, L.-I. Bulyk, V. Tsiumra, J. Barzowska, P. Xiong, A. Lysak, Y. Zhydachevskyy, and A. Suchocki, High-pressure near-infrared luminescence studies of Fe^{3+} -activated LiGaO_2 , *Inorg. Chem.* **62**, 12434 (2023).
- [10] S. Panda, P. Vinodkumar, M. Sahoo, U. Madhusoodanan, and B. Panigrahi, Probing the site occupancy of dopants in deep red-NIR emitting $\text{LiAl}_5\text{O}_8:\text{Eu}^{3+}, \text{Cr}^{3+}$ and Fe^{3+} nano phosphors using photoluminescence and X-ray absorption spectroscopy, *J. Alloys Compd.* **857**, 157615 (2021).
- [11] J. Neto, T. Abritta, F. de S. Barros, and N. Melamed, A comparative study of the optical properties of Fe^{3+} in ordered LiGa_5O_8 and LiAl_5O_8 , *J. Lumin.* **22**, 109 (1981).
- [12] C. McShera, P. Colleran, T. Glynn, G. Imbusch, and J. Remeika, Luminescence study of $\text{LiGa}_{5-x}\text{Fe}_x\text{O}_8$, *J. Lumin.* **28**, 41 (1983).

- [13] N. Zhang, H. Liu, Q. Sai, C. Shao, C. Xia, L. Wan, Z. C. Feng, and H. F. Mohamed, Structural and electronic characteristics of Fe-doped β -Ga₂O₃ single crystals and the annealing effects, *J. Mater. Sci.* **56**, 13178 (2021).
- [14] R. Stoyanova, A.-L. Barra, M. Yoncheva, E. Kuzmanova, and E. Zhecheva, Local structure of Mn⁴⁺ and Fe³⁺ spin probes in layered LiAlO₂ oxide by modelling of zero-field splitting parameters, *Dalton Trans.* **40**, 9106 (2011).
- [15] N. Pathak, S. K. Gupta, K. Sanyal, M. Kumar, R. M. Kadam, and V. Natarajan, Photoluminescence and EPR studies on Fe³⁺ doped ZnAl₂O₄: An evidence for local site swapping of Fe³⁺ and formation of inverse and normal phase, *Dalton Trans.* **43**, 9313 (2014).
- [16] Q. Chen, C. Ji, and C.-K. Duan, Luminescence of iron ions in crystals: Site occupancy, valence states, and excited-state properties, *Phys. Rev. B* **109**, 165124 (2024).
- [17] K. Eigenmann, K. Kurtz, and H. Günthard, The optical spectrum of α -Al₂O₃:Fe³⁺, *Chem. Phys. Lett.* **13**, 54 (1972).
- [18] A. Y. Polyakov, N. B. Smirnov, I. V. Schemerov, A. V. Chernykh, E. B. Yakimov, A. I. Kochkova, A. N. Tereshchenko, and S. J. Pearton, Electrical properties, deep levels and luminescence related to Fe in bulk semi-insulating β -Ga₂O₃ doped with Fe, *ECS J. Solid State Sci. Technol.* **8**, Q3091 (2019).
- [19] K. Blazey, Optical absorption of MgO: Fe, *J. Phys. Chem. Solids* **38**, 671 (1977).
- [20] N. T. Melamed, J. Neto, T. Abritta, and F. de Souza Barros, A comparison of the luminescence of LiAl₅O₈: Fe and LiGa₅O₈: Fe—II. Fe³⁺ in octahedral sites, *J. Lumin.* **24-25**, 249 (1981).
- [21] K.-W. Zhou, J.-K. Xie, Y.-M. Ning, S.-B. Zhao, and P.-F. Wu, Crystal-field theory and the S-state splitting of Fe³⁺ in yttrium gallium garnet, *Phys. Rev. B* **44**, 7499 (1991).
- [22] G. B. Scott, D. E. Lacklison, and J. L. Page, Absorption spectra of Y₃Fe₅O₁₂ (YIG) and Y₃Ga₅O₁₂: Fe³⁺, *Phys. Rev. B* **10**, 971 (1974).
- [23] J. Zeng, G. Peng, S. Zhang, G. Krishnan R, G. Ju, Y. Li, and Y. Hu, In-situ Insights into trap attributions in Fe³⁺-activated long persistent phosphors, *J. Lumin.* **232**, 117810 (2021).
- [24] R. Kuang, H. Lian, Y. Zhu, S. Gu, L. Huang, B.-M. Liu, and J. Wang, Designing Photochromic materials La₂MgSnO₆:Er, Fe with dynamic luminescence modulation for dual-mode optical information reading, *Adv. Opt. Mater.* **12**, 2400045 (2024).
- [25] S. Su, C. Hu, S. Ding, Y. Sun, L. Sun, Y. Zou, R. Liu, Z. Lei, B. Teng, and D. Zhong, Achieving broadband NIR emission in Fe³⁺-activated ALaBB'O₆ (A = Ba, Sr, Ca; B-B' = Li-Te, Mg-Sb) Phosphors via Multi-Site Ionic Co-Substitutions, *Adv. Opt. Mater.* **12**, 2302383 (2023).
- [26] J. Su, R. Pang, T. Tan, S. Wang, X. Chen, S. Zhang, and H. Zhang, A novel near-infrared emitting Sr₂LuSbO₆:Fe³⁺ phosphor with persistent luminescence performance, *Adv. Opt. Mater.* **12**, 2303187 (2024).
- [27] X. Zhang, D. Chen, X. Chen, C. Zhou, P. Chen, Q. Pang, and L. Zhou, Broadband near-infrared luminescence from Fe³⁺-activated NaScSi₂O₆ phosphors for luminescence thermometry and night-vision applications, *Dalton Trans.* **51**, 14243 (2022).
- [28] G. Kresse and J. Hafner, Ab initio molecular dynamics for liquid metals, *Phys. Rev. B* **47**, 558 (1993).
- [29] G. Kresse and J. Hafner, Ab initio molecular-dynamics simulation of the liquid-metal–amorphous–semiconductor transition in germanium, *Phys. Rev. B* **49**, 14251 (1994).
- [30] P. E. Blöchl, Projector augmented-wave method, *Phys. Rev. B* **50**, 17953 (1994).
- [31] J. P. Perdew, K. Burke, and M. Ernzerhof, Generalized gradient approximation made simple, *Phys. Rev. Lett.* **77**, 3865 (1996).
- [32] See Supplemental Material at <http://link.aps.org/supplemental/10.1103/PhysRevMaterials.8.095201> for Note 1: The effect of configuration interaction on ⁴T₁ and ²T₂, Note 2: The Δ/B values of tetrahedral and octahedral Fe³⁺ activators by first principles calculations, which includes Refs. [33–39].
- [33] B. J. Wood, R. J. Kirkpatrick, and B. Montez, Order-disorder phenomena in MgAl₂O₄ spinel, *Am. Mineral.* **71**, 999 (1986).
- [34] J. Sappl, F. Jung, and C. Hoch, Facile one-step syntheses of several complex ionic lithium gallates from LiGa as intermetallic precursors, *Chem. Mater.* **32**, 866 (2020).
- [35] S. J. Kim, Z. C. Chen, and A. V. Virkar, Phase transformation kinetics in the doped system LiAl₅O₈-LiFe₅O₈, *J. Am. Ceram. Soc.* **71**, C428 (1988).
- [36] D. Rodic, M. Mitric, R. Tellgren, and H. Rundlof, The cation distribution and magnetic structure of Y₃Fe_{5-x}Al_xO₁₂, *J. Magn. Magn. Mater.* **232**, 1 (2001).
- [37] A. Verma, N. Malhan, and A. K. Ganguli, Preparation, structure and characterization of nanocrystalline-Nd:Y₃Ga₅O₁₂, *Mater. Lett.* **81**, 242 (2012).
- [38] X. Liu, L. Zhu, L. Wang, C. Yu, and J. Lin, Synthesis and Luminescent Properties of Lu₃Ga₅O₁₂:RE³⁺ (RE = Eu, Tb, and Pr) Nanocrystalline Phosphors via Sol-Gel Process, *J. Electrochem. Soc.* **155**, P21 (2008).
- [39] A. Faik, D. Orobengoa, E. Iturbe-Zabalzo, and J. Igartua, A study of the crystal structures and the phase transitions of the ordered double perovskites Sr₂ScSbO₆ and Ca₂ScSbO₆, *J. Solid State Chem.* **192**, 273 (2012).
- [40] H. Hsu, P. Blaha, M. Cococcioni, and R. M. Wentzcovitch, Spin-state crossover and hyperfine interactions of ferric iron in MgSiO₃ perovskite, *Phys. Rev. Lett.* **106**, 118501 (2011).
- [41] K. Kniec, W. Piotrowski, K. Ledwa, L. D. Carlos, and L. Marciniak, Spectral and thermometric properties altering through crystal field strength modification and host material composition in luminescence thermometers based on Fe³⁺ doped AB₂O₄ type nanocrystals (A = Mg, Ca; B = Al, Ga), *J. Mater. Chem. C* **9**, 517 (2021).
- [42] Q. Chen, L. Shang, C.-G. Ma, and C.-K. Duan, Angular Jahn–Teller effect and photoluminescence of the tetrahedral coordinated Mn²⁺ activators in solids—A first-principles study, *Inorg. Chem.* **61**, 13471 (2022).
- [43] J. P. Perdew, A. Ruzsinszky, L. A. Constantin, J. Sun, and G. I. Csonka, Some fundamental issues in ground-state density functional theory: A guide for the perplexed, *J. Chem. Theory Comput.* **5**, 902 (2009).
- [44] S. Sugano, *Multiplets of Transition-Metal Ions in Crystals* (Academic Press, New York, 2012).
- [45] X. Zhou, X. Luo, B. Wu, S. Jiang, L. Li, X. Luo, and Y. Pang, The broad emission at 785 nm in YAG:Ce³⁺, Cr³⁺ phosphor, *Spectrochim. Acta A: Mol. Biomol. Spectrosc.* **190**, 76 (2018).
- [46] K. Kniec, K. Ledwa, K. Maciejewska, and L. Marciniak, Intentional modification of the optical spectral response and relative sensitivity of luminescent thermometers based on Fe³⁺, Cr³⁺, Nd³⁺ co-doped garnet nanocrystals by crystal field strength optimization, *Mater. Chem. Front.* **4**, 1697 (2020).
- [47] M. Yeerlan, M. Zhang, and P. Dai, Near-unity quantum efficiency wavelength-tunable nir phosphors

- ($\text{Sr}_{2-y}\text{Ca}_y$) $\text{Sc}_{1-x}\text{SbO}_6$: $x\text{Fe}^{3+}$ with excellent thermal stability, *J. Am. Ceram. Soc.* **107**, 5588 (2024).
- [48] L. Sosman, A. López, S. Pedro, and A. Papa, Photoluminescence of the $\text{Mg}_2\text{Al}_4\text{Si}_5\text{O}_{18}$ - Al_2O_3 - MgAl_2O_4 - SiO_2 ceramic system containing Fe^{3+} and Cr^{3+} as impurity ions, *Opt. Mater.* **76**, 353 (2018).
- [49] E. Cavalli, A. Belletti, and E. Zannoni, Luminescence of Fe-doped willemite single crystals, *J. Solid State Chem.* **117**, 16 (1995).
- [50] T. Abritta, N. Melamed, J. Neto, and F. De Souza Barros, The optical properties of Cr^{3+} in LiAl_5O_8 and LiGa_5O_8 , *J. Lumin.* **18-19**, 179 (1979).
- [51] K. Izumi, S. Miyazaki, S. Yoshida, T. Mizokawa, and E. Hanamura, Optical properties of $3d$ transition-metal-doped MgAl_2O_4 spinels, *Phys. Rev. B* **76**, 075111 (2007).
- [52] N. Basavaraju, K. R. Priolkar, D. Gourier, S. K. Sharma, A. Bessière, and B. Viana, The importance of inversion disorder in the visible light induced persistent luminescence in Cr^{3+} doped AB_2O_4 ($A = \text{Zn}$ or Mg and $B = \text{Ga}$ or Al), *Phys. Chem. Chem. Phys.* **17**, 1790 (2015).
- [53] O. Q. De Clercq, L. I. D. J. Martin, K. Korthout, J. Kusakovskij, H. Vrielinck, and D. Poelman, Probing the local structure of the near-infrared emitting persistent phosphor LiGa_5O_8 : Cr^{3+} , *J. Mater. Chem. C* **5**, 10861 (2017).
- [54] G. Pott and B. McNicol, The luminescence of Fe^{3+} and Cr^{3+} IN α -gallia, *J. Lumin.* **6**, 225 (1973).
- [55] G. O'Connor, C. McDonagh, and T. Glynn, Luminescence from Fe^{3+} ions in octahedral sites in LiGa_5O_8 , *J. Lumin.* **48-49**, 545 (1991).
- [56] W. Zhao, L. Li, Z. Wu, Y. Wang, Z. Cao, F. Ling, S. Jiang, G. Xiang, X. Zhou, and Y. Hua, Bifunctional near-infrared-emitting phosphors of chromium (iii)-activated antimonates for nir light-emitting diodes and low-temperature thermometry, *J. Alloys Compd.* **965**, 171370 (2023).
- [57] J. Xu, J. Ueda, and S. Tanabe, Toward tunable and bright deep-red persistent luminescence of Cr^{3+} in garnets, *J. Am. Ceram. Soc.* **100**, 4033 (2017).
- [58] A. Vink and A. Meijerink, Electron-phonon coupling of Cr^{3+} doped garnets, *J. Phys. Chem. Solids* **61**, 1717 (2000).
- [59] C. Li and J. Zhong, Highly efficient broadband near-infrared luminescence with zero-thermal-quenching in garnet $\text{Y}_3\text{In}_2\text{Ga}_3\text{O}_{12}$: Cr^{3+} Phosphors, *Chem. Mater.* **34**, 8418 (2022).
- [60] E. Raudonyte, H. Bettentrup, D. Uhlich, S. Sakirzanovas, O. Opuchovic, S. Tautkus, and A. Katelnikovas, On the $\text{Ce}^{3+} \rightarrow \text{Cr}^{3+}$ energy transfer in $\text{Lu}_3\text{Al}_5\text{O}_{12}$ garnets, *Opt. Mater.* **37**, 204 (2014).
- [61] X. Yang, W. Chen, D. Wang, X. Chai, G. Xie, Z. Xia, M. S. Molocheev, Y. Liu, and B. Lei, Near-infrared photoluminescence and phosphorescence properties of Cr^{3+} -Doped garnet-type $\text{Y}_3\text{Sc}_2\text{Ga}_3\text{O}_{12}$, *J. Lumin.* **225**, 117392 (2020).
- [62] L. Zhang, S. Zhang, Z. Hao, X. Zhang, G.-h. Pan, Y. Luo, H. Wu, and J. Zhang, A high efficiency broad-band near-infrared $\text{Ca}_2\text{LuZr}_2\text{Al}_3\text{O}_{12}$: Cr^{3+} garnet phosphor for blue LED chips, *J. Mater. Chem. C* **6**, 4967 (2018).
- [63] F. Zhao, H. Cai, Z. Song, and Q. Liu, Structural confinement for Cr^{3+} activators toward efficient near-infrared phosphors with suppressed concentration quenching, *Chem. Mater.* **33**, 3621 (2021).
- [64] F. Zhao, H. Cai, S. Zhang, Z. Song, and Q. Liu, Octahedron-dependent near-infrared luminescence in Cr^{3+} -activated phosphors, *Mater. Today Chem.* **23**, 100704 (2022).
- [65] G. J. Dirksen, A. N. J. M. Hoffman, T. P. van de Bout, M. P. G. Laudy, and G. Blasse, Luminescence spectra of pure and doped GaBO_3 and LiGaO_2 , *J. Mater. Chem.* **1**, 1001 (1991).
- [66] Q. Shao, H. Ding, L. Yao, J. Xu, C. Liang, and J. Jiang, Photoluminescence properties of a ScBO_3 : Cr^{3+} phosphor and its applications for broadband near-infrared LEDs, *RSC Adv.* **8**, 12035 (2018).
- [67] L. Qiu, P. Wang, J. Mao, Z. Liao, F. Chi, Y. Chen, X. Wei, and M. Yin, Cr^{3+} -Doped InTaO_4 phosphor for multi-mode temperature sensing with high sensitivity in a physiological temperature range, *Inorg. Chem. Front.* **9**, 3187 (2022).
- [68] J. Zhong, Y. Zhuo, F. Du, H. Zhang, W. Zhao, S. You, and J. Brgoch, Efficient broadband near-infrared emission in the GaTaO_4 : Cr^{3+} phosphor, *Adv. Opt. Mater.* **10**, 2101800 (2022).